Article

Dipolar evaporation of reactive molecules to below the Fermi temperature

https://doi.org/10.1038/s41586-020-2980-7

Received: 20 July 2020

Accepted: 29 September 2020

Published online: 9 December 2020

Check for updates

Giacomo Valtolina[1,2]✉, Kyle Matsuda[1,2], William G. Tobias[1,2], Jun-Ru Li[1,2], Luigi De Marco[1,2] & Jun Ye[1,2]✉

The control of molecules is key to the investigation of quantum phases, in which rich degrees of freedom can be used to encode information and strong interactions can be precisely tuned[1]. Inelastic losses in molecular collisions[2–5], however, have greatly hampered the engineering of low-entropy molecular systems[6]. So far, the only quantum degenerate gas of molecules has been created via association of two highly degenerate atomic gases[7,8]. Here we use an external electric field along with optical lattice confinement to create a two-dimensional Fermi gas of spin-polarized potassium–rubidium (KRb) polar molecules, in which elastic, tunable dipolar interactions dominate over all inelastic processes. Direct thermalization among the molecules in the trap leads to efficient dipolar evaporative cooling, yielding a rapid increase in phase-space density. At the onset of quantum degeneracy, we observe the effects of Fermi statistics on the thermodynamics of the molecular gas. These results demonstrate a general strategy for achieving quantum degeneracy in dipolar molecular gases in which strong, long-range and anisotropic dipolar interactions can drive the emergence of exotic many-body phases, such as interlayer pairing and p-wave superfluidity.

The complex internal structure of molecules can be both useful and a hindrance: it represents a key resource for the development of tunable and programmable quantum devices[1,9,10], but it is also responsible for strong inelastic losses during collisions[11–14]. Despite recent advances in molecular quantum science[15–24], full control of elastic collisions between molecules has not been achieved, making it very difficult to create the low-entropy bulk molecular gases that are required for the exploration of rich many-body physics and emergent quantum phenomena[1,25].

Here, we report the realization of highly tunable elastic interactions in a quantum gas of polar molecules through the application of an external electric field along a stack of two-dimensional (2D) layers generated with a one-dimensional optical lattice. The induced electric dipole moment in the laboratory frame gives rise to repulsive dipolar interactions that stabilize the molecular gas against reactive collisions and formation of collisional complexes. These long-range interactions provide a large elastic collision cross-section for identical ultracold fermionic molecules, in contrast to contact interactions[26]. We demonstrate the enhancement of dipolar interactions by several orders of magnitude and achieve a ratio of elastic-to-inelastic collisions that exceeds 100. This favourable interaction regime enables direct molecular thermalization and efficient evaporative cooling, allowing us to bring the molecular temperature T below the Fermi temperature T_F. The onset of quantum degeneracy is signalled by deviations from the classical expansion energy as the ratio T/T_F is reduced below unity[7,27].

Our strategy follows previous theory proposals[28–30] and our earlier experimental study on molecular reactions in quasi-two dimensions[31]. This geometry allows us to take advantage of the anisotropic character of the dipolar potential and retain only the repulsive side-to-side dipole–dipole interactions within each 2D site, while preventing the attractive head-to-tail interactions that facilitate losses at short range. Our recent advances in the production of degenerate Fermi gases of polar molecules[7,8], combined with precise electric-field control using in-vacuum electrodes[32] (Fig. 1), allow us to perform a systematic characterization of the properties of a 2D Fermi gas of polar molecules.

A long-lived 2D Fermi gas of polar molecules

The KRb 2D Fermi gas is created from an ultracold atomic mixture of fermionic ^{40}K and bosonic ^{87}Rb atoms. The atomic mixture is initially held in a crossed optical dipole trap (ODT) and then transferred into a single layer of a large-spacing lattice (LSL) with an 8-μm spatial period, which increases the mixture's confinement along the vertical direction ($\mathbf{y}$). The mixture is then transferred into a vertical lattice (VL) with spacing of 540 nm that confines it to a quasi-2D geometry. The intermediate LSL transfer results in the Rb cloud populating a controllable number of VL layers τ ranging between 5 and 15. We directly probe the number of occupied 2D layers via a matter-wave focusing technique on the Rb cloud (Fig. 1c)[33,34]. The measured τ is in excellent agreement with theoretical modelling of the in situ cloud size (see Methods).

Magneto-optical association is used to pair roughly half of the initial Rb atoms into ground-state KRb molecules[35]. This process is fast and coherent, and the resulting molecular cloud populates the same layers originally occupied by the Rb cloud. The leftover K and Rb atoms are selectively and quickly removed from the trap. In the VL, the trap frequencies are set to $(\omega_x, \omega_y, \omega_z) = 2\pi \times (40, 17{,}000, 40)$ Hz. The quoted trapping frequencies are for KRb throughout the paper unless otherwise

[1]JILA, National Institute of Standards and Technology, Boulder, CO, USA. [2]Department of Physics, University of Colorado, Boulder, CO, USA. ✉e-mail: giva4289@colorado.edu; ye@jila.colorado.edu

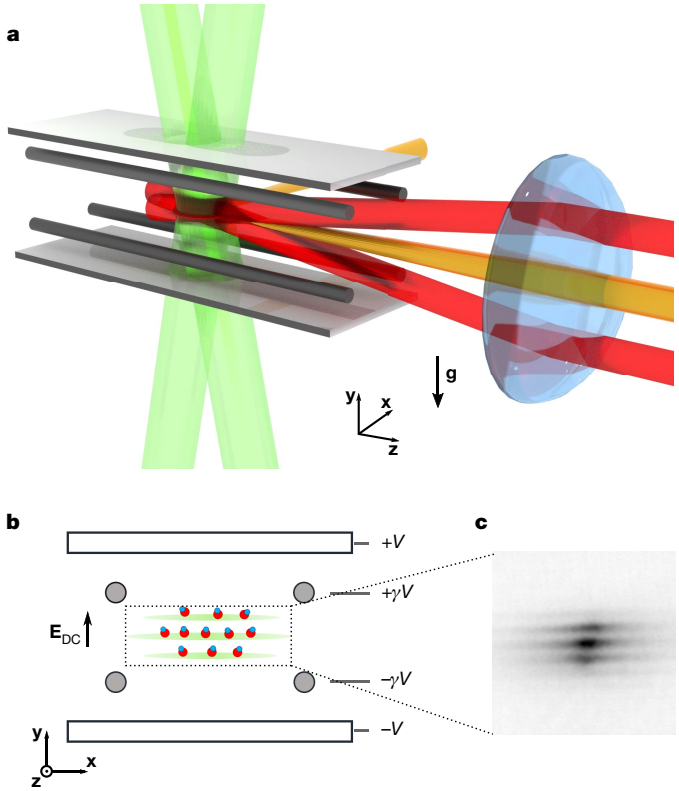

Fig. 1 | Experimental setup. a, The 2D molecular cloud is trapped at the centre of the electrode assembly (grey). 2D optical trapping is achieved with the VL (green), which is loaded using the ODT (orange) and LSL (red). Absorption images of molecules are collected through the same lens as that used to focus the LSL. **b**, Sketch of the experiment as seen down the *z* axis. The bias electric field is generated along **y**, perpendicular to the 2D layers of the VL. **c**, Matter-wave focusing data of the Rb layers in the VL, which have a spacing of 540 nm.

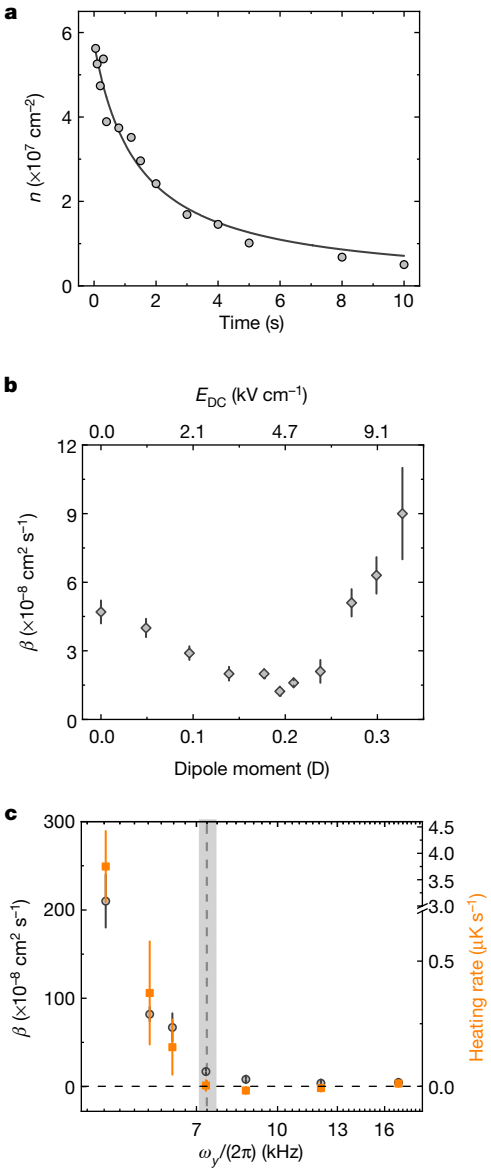

Fig. 2 | Long-lived polar molecules in 2D. a, Time evolution of the molecular density n at $d = 0.2$ D. **b**, Inelastic loss rate β as a function of dipole moment. All error bars are 1 standard error of the mean (s.e.), determined from two-body decay fits (equation (1)) The top x axis shows the bias electric field E_{DC} at the corresponding dipole moment . **c**, Both β (grey circles) and the heating rate (orange squares) saturate at their minimum values near $\omega_y = 2\pi \times 7$ kHz (vertical grey bar indicates uncertainty in the molecule temperature), consistent with the mechanism of quasi-2D dipolar scattering. Heating rate error bars are 1 s.e., determined from linear fits.

stated. We create a 2D gas with $N \approx 20{,}000$ trapped molecules, a typical temperature $T \approx 250$ nK, and T/T_F ranging from 1.5 to 3 depending on τ.

The 2D molecular cloud is at the centre of an in-vacuum six-electrode assembly composed of two indium tin oxide (ITO)-coated glass plates and four tungsten rods (Fig. 1a). With this, we generate a highly tunable bias electric field E_{DC} that induces strong dipolar interactions between molecules (Fig. 1b). The ratio γ of the voltage of the rods to the voltage of the plates can be used to cancel the curvature introduced by the parallel plate edges (flat-field configuration) or to introduce additional curvatures and gradients for molecule manipulation.

The chemically reactive KRb molecules suffer from inelastic two-body losses[2,12], which result in the average molecular density n decaying over time t according to a two-body rate equation of the form:

$$\frac{\mathrm{d}n}{\mathrm{d}t} = -\beta n^2 + \frac{\partial n}{\partial T}\frac{\mathrm{d}T}{\mathrm{d}t}, \quad (1)$$

where β is the two-body loss rate coefficient and the second term on the right side of equation (1) accounts for temperature changes affecting the density[3].

In a three-dimensional (3D) harmonic trap, β increases sharply with E_{DC}, so that inelastic interactions dominate elastic ones[3,36]. However, strong confinement along the direction of E_{DC} suppresses this detrimental loss increase[31] by preventing head-to-tail collisions along E_{DC}. Even though n is large in the occupied layers, the molecular gas shows a remarkable stability with repulsive interactions turned on. With an induced dipole moment $d = 0.2$ D in the flat-field configuration, KRb molecules survive for several seconds (Fig. 2a). The evolution of β as a function of E_{DC} is shown in Fig. 2b. Close to $E_{DC} = 4.7$ kV cm^{-1}, β reaches a minimum of nearly five times below the zero-field value. The increase of β for $d > 0.2$ D is consistent with a quasi-2D picture of dipolar scattering[37,38].

To understand the effect of optical confinement, we perform a thorough characterization of the 3D-to-2D crossover by measuring β versus ω_y at $E_{DC} = 5$ kV cm^{-1} (Fig. 2c). Here, β drops abruptly as the lattice vertical confinement is increased and reaches a plateau near $\omega_y = 2\pi \times 7$ kHz, corresponding to the quasi-2D limit where $k_B T \lesssim \hbar\omega_y$, with k_B being the Boltzmann constant and $\hbar$ the reduced Planck constant, and the molecules principally occupy the lowest band of the VL. In contrast to the 3D case, where the heating rate exceeds 3 μK s^{-1}, in quasi-two dimensions we do not record a substantial increase in temperature along the

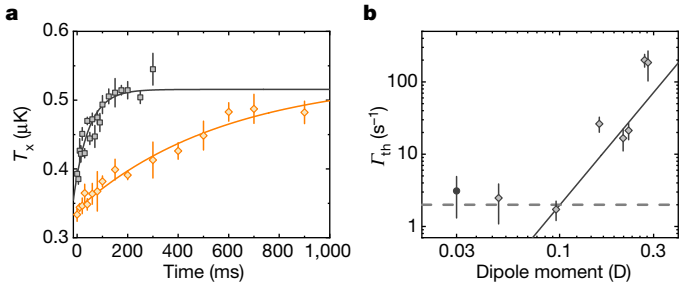

Fig. 3 | Tuning strong dipolar elastic interactions in a 2D molecular gas. **a**, Cross-dimensional thermalization dynamics at $d = 0.1$ D (orange diamonds) and $d = 0.21$ D (grey squares). Error bars are 1 s.e. of 5 independent measurements. **b**, The trend of Γ_{th} extracted from cross-dimensional thermalization dynamics as a function of d. The solid line is a power-law fit for $d \geq 0.1$ D that yields a power of 3.3(1.0). The filled grey circle corresponds to the measurement at $d = 0.0$ D, and it is artificially placed at $d = 0.03$ D for figure clarity. The dashed horizontal line at $\Gamma_{th} = 2\ s^{-1}$ is the background cross-dimensional relaxation from trap anharmonicity. All error bars are 1 s.e., determined from exponential fits.

radial direction. The suppression of heating is due to cancellation of anti-evaporation in quasi-two dimensions[30] and represents another advantage of this configuration.

Cross-dimensional thermalization

To characterize elastic interactions in our thermal molecular cloud, we perform cross-dimensional thermalization at various values of E_{DC}. We diabatically change the power in one of the ODT beams to suddenly increase the energy along **z**. Elastic collisions between the molecules then redistribute the excess energy from **z** onto **x**. The rate Γ_{th} of the temperature equilibration between the two axes is proportional to the dipolar elastic collision rate[28,39,40]. We extract Γ_{th} by fitting the increase of T along **x** with an exponential curve.

With the loss suppressed in quasi-2D, we expect a substantial increase of the thermalization rate Γ_{th} with a d^4 dependence[28,30]. Comparing the thermalization dynamics observed for $d = 0.1$ D and 0.21 D (Fig. 3a), we see Γ_{th} increase by a factor of 10. Over our investigated range of E_{DC}, Γ_{th} changes by two orders of magnitude (Fig. 3b), showing the extreme tunability of elastic dipolar interactions in our system. We observe the cross-dimensional thermalization dynamics at lower dipolar strength ($d < 0.1$ D) being dominated by cross-dimensional relaxation owing to trap anharmonicity, which limits the smallest Γ_{th} that we can measure. For $d \geq 0.1$ D, a fit to a power-law dependence of Γ_{th} on d yields a power of 3.3 ± 1.0, in good agreement with theoretical expectations[28,30]. For the highest values of d we explored, the rate Γ_{th} is comparable to the radial trapping frequency, opening the way for future studies of collective dynamics in molecular gases[41].

An estimate of the ratio of elastic-to-inelastic collisions is obtained by comparing Γ_{th} to the initial rate of inelastic losses Γ_{in}, which is expressed as $\Gamma_{in} = \beta n_0$, with n_0 the initial average density of the 2D gas. From the data in Fig. 2b, at $d = 0.2$ D, we estimate a rate $\Gamma_{in} = 0.83(5)\ s^{-1}$, whereas $\Gamma_{th} = 21(6)\ s^{-1}$ for the same dipole strength. In the temperature regime of the cross-dimensional thermalization experiments, theoretical models[30] predict that $\alpha = 8$ elastic collisions are needed for each molecule to reach thermal equilibrium. This indicates a ratio of elastic-to-inelastic collisions $\alpha(\Gamma_{th}/\Gamma_{in}) = 200 \pm 60$, demonstrating that elastic processes dominate in this system.

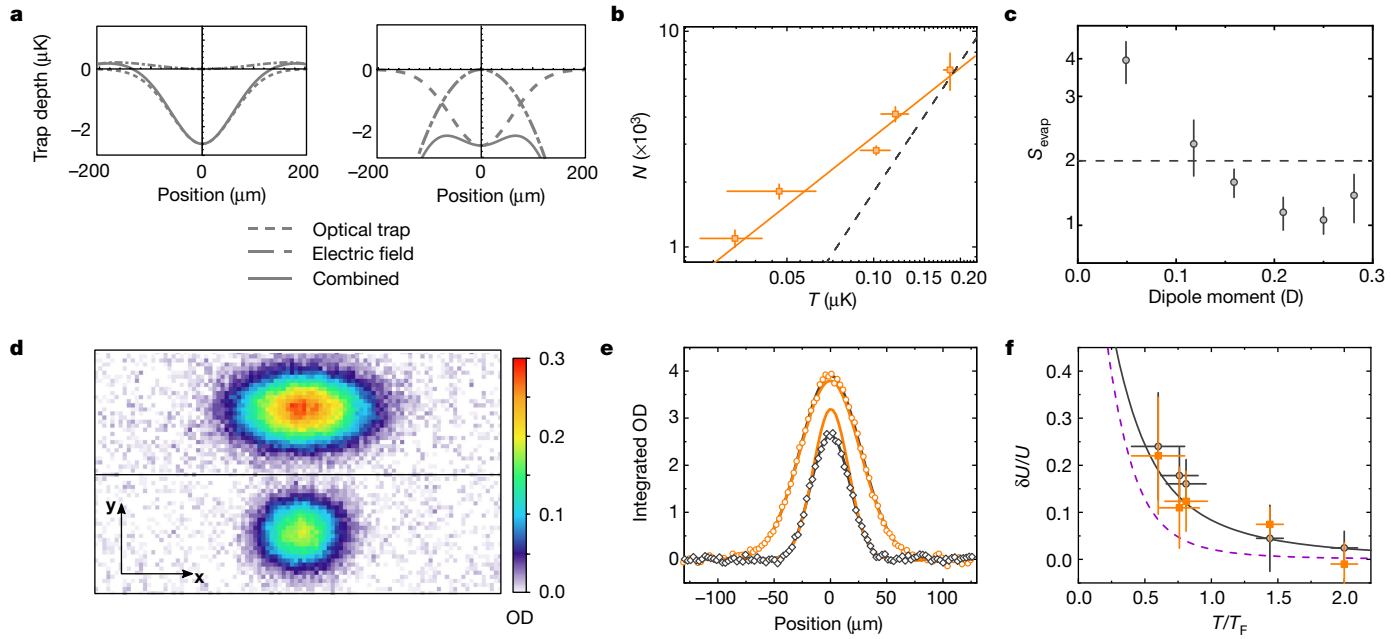

Fig. 4 | Evaporative cooling to the quantum degenerate regime. **a**, Cuts along the x axis of the combined electro-optical potential for the flat-field configuration (left panel) and at the end of the evaporation (right panel). **b**, Evolution of N and T (orange squares) at different stages of the evaporation trajectory at $E_{DC} = 6.5\ kV\ cm^{-1}$ and $d = 0.25$ D. The power-law fit (orange line) yields $S_{evap} = 1.06(15)$. The dashed grey line is for a constant T/T_F, corresponding to $S_{evap} = 2.0$. Error bars are 1 s.e. of four independent measurements. **c**, Summary of S_{evap} versus d. All error bars are 1 s.e., determined from power-law fits. **d**, Average of 20 band-mapped absorption images of the molecular cloud in the x–y plane after 5.84 ms of time of flight for $T/T_F = 2.0(1)$ (top) and $T/T_F = 0.81(15)$ (bottom). **e**, Optical density (OD, dimensionless) profiles (orange circles for $T/T_F = 2.0(1)$ and grey diamonds for $T/T_F = 0.81(15)$) of the images in **d** (integrated along **y**), together with the Fermi–Dirac fit to the whole cloud (grey line) and the Gaussian fit to the outer wings (orange line). **f**, Measurement of $\delta U/U$ at different values of T/T_F from the Fermi–Dirac fit to the entire cloud (grey circles) and from the Gaussian fit to the outer wings of the cloud (orange squares). The solid and dashed curves show $\delta U/U$ for the 2D and 3D ideal Fermi gases, respectively. All error bars are 1 s.e., determined from Gaussian or polylogarithmic fits.

Electric-field-controlled evaporative cooling

The large elastic-to-inelastic collision ratio is an excellent setting for evaporatively cooling to enhance the phase-space density of our molecular cloud. For non-degenerate 2D fermionic gases, phase-space density is inversely proportional to $(T/T_F)^2$, and phase-space density increases only if the change of N versus T during evaporation fulfills the criterion:

$$S_{evap} = \frac{\partial \log N}{\partial \log T} < 2. \quad (2)$$

When $S_{evap} = 2$, the gas maintains a constant T/T_F.

The efficiency of evaporative cooling relies on our ability to selectively remove the hottest molecules from the trap and to let the remaining molecules re-thermalize to a lower temperature. Reducing the trap depth by lowering the optical trap power for evaporation, as is routinely done in ultracold atom experiments, is not a viable solution here because we cannot lower the tight 2D confinement without affecting the stability of the cloud (Fig. 2c). Instead, by increasing γ with respect to the flat-field configuration, we introduce a tunable anti-trapping electric field along the x direction to reduce the radial confinement experienced by the molecules (Fig. 4a). By measuring the change of ω_x as a function of γ, we can directly reconstruct the combined electro-optical potential and benchmark its theoretical modelling (see Extended Data Fig. 2).

For the evaporation measurement, we start with a 2D gas with layer number $\tau = 5 \pm 1$, $\omega_y = 2\pi \times 17$ kHz, and an average $T/T_F = 1.5(1)$. After creating the molecules (see Methods), we ramp E_{DC} to a target field while keeping γ at the flat-field value. We trigger the evaporation by increasing γ to reduce the trap depth. We do not observe any evaporation until the truncation parameter η, defined as the ratio of trap depth over thermal energy $k_B T$, reaches a value of 4 (see Methods), in good agreement with theoretical expectations[30]. We further increase γ over a timescale of hundreds of milliseconds, which is long enough for the molecules to efficiently re-thermalize at a lower T as the trap depth is reduced. At the end of the evaporation ramp, we return to the flat-field configuration and ramp E_{DC} back to its initial value. We coherently convert the ground state molecules back to the Feshbach state and image the cloud of Feshbach molecules after band-mapping from the VL. Detailed time sequences for the evolution of E_{DC}, γ and trap depth are shown in the Methods.

At $E_{DC} = 6.5\,\mathrm{kV\,cm^{-1}}$, the evolution of N and T at different stages of the optimized evaporation sequence is shown in Fig. 4b. To characterize the evaporation efficiency, we fit the N versus T dependence with a power-law function to extract S_{evap}. For the data shown in Fig. 4b, we obtain $S_{evap} = 1.06(15)$, far below the threshold of 2 required to increase phase-space density. The trend of S_{evap} versus d is plotted in Fig. 4c and reaches a minimum (that is, maximum increase in phase-space density) at $d = 0.25$ D, where the ratio of elastic-to-inelastic collisions is the largest[37,38].

When we cool molecules to $T < T_F$ (Fig. 4d), we witness the onset of Fermi degeneracy, which is signalled by deviations from classical thermodynamics owing to the increasing role of the Pauli exclusion principle. Here, $T_F = \frac{\hbar\omega_R}{k_B}\left(\frac{2N}{\tau}\right)^{1/2}$, with $\omega_R = \sqrt{\omega_x \omega_z}$ the geometric mean of the radial trapping frequency. Our best result produced a 2D molecular Fermi gas with $N = 1.7(1) \times 10^3$ and $T/T_F = 0.6(2)$.

We extract T by using either a fit to the Fermi–Dirac distribution on the entire expanded cloud or a Gaussian fit restricted to the cloud's outer wings (see Methods). As shown in Fig. 4e, for $T/T_F = 0.81(15)$ the Gaussian fit to the outer wings of the time of flight density profile overestimates the density at the centre. We quantify this through the increasing difference $\delta U = U - U_{cl}$ between the energy U of the fermionic gas and the energy $U_{cl} \propto k_B T$, as T/T_F decreases[7,27]. U is determined from a Gaussian fit to the whole cloud (see Methods) and U_{cl} is calculated based on the measured T. Owing to the different density of states in the harmonic trap, the chemical potential crosses zero for $T/T_F = 0.78$ for the 2D case, in contrast to 0.57 for the 3D case. Correspondingly, the 2D Fermi gas shows a larger δU with respect to the 3D case at the same T/T_F (ref. [42]). As we reach $T < T_F$, in excellent agreement with theoretical expectations, we observe a large increase of δU (Fig. 4f). This is a hallmark for the onset of quantum degeneracy in trapped Fermi gases[27].

Conclusions

We have realized a 2D Fermi gas of reactive polar molecules where precisely tunable elastic dipolar interactions dominate all inelastic processes. This allowed us to perform evaporative cooling of molecules to the onset of Fermi degeneracy. We demonstrated a general and robust scheme for ultracold gases of polar molecules to reach quantum degeneracy. For example, using a strong 2D confinement and large dipolar interactions, this method should enable Bose–Einstein condensation in bosonic molecular gases. It has long been anticipated that quantum gases of polar molecules in two dimensions would allow access to strongly correlated many-body phases[43–52]. Our results set the stage for exploration of these exotic regimes.

Online content

Any methods, additional references, Nature Research reporting summaries, source data, extended data, supplementary information, acknowledgements, peer review information; details of author contributions and competing interests; and statements of data and code availability are available at https://doi.org/10.1038/s41586-020-2980-7.

1. Bohn, J. L., Rey, A. M. & Ye, J. Cold molecules: progress in quantum engineering of chemistry and quantum matter. *Science* **357**, 1002–1010 (2017).
2. Ospelkaus, S. et al. Quantum-state controlled chemical reactions of ultracold potassium-rubidium molecules. *Science* **327**, 853–857 (2010).
3. Ni, K.-K. et al. Dipolar collisions of polar molecules in the quantum regime. *Nature* **464**, 1324–1328 (2010).
4. Guo, M. et al. Dipolar collisions of ultracold ground-state bosonic molecules. *Phys. Rev. X* **8**, 041044 (2018).
5. Gregory, P. D. et al. Sticky collisions of ultracold RbCs molecules. *Nat. Commun.* **10**, 3104 (2019).
6. Moses, S. A. et al. Creation of a low-entropy quantum gas of polar molecules in an optical lattice. *Science* **350**, 659–662 (2015).
7. De Marco, L. et al. A degenerate Fermi gas of polar molecules. *Science* **363**, 853–856 (2019).
8. Tobias, W. G. et al. Thermalization and sub-Poissonian density fluctuations in a degenerate molecular Fermi gas. *Phys. Rev. Lett.* **124**, 033401 (2020).
9. André, A. et al. A coherent all-electrical interface between polar molecules and mesoscopic superconducting resonators. *Nat. Phys.* **2**, 636–642 (2006).
10. DeMille, D., Doyle, J. M. & Sushkov, A. O. Probing the frontiers of particle physics with tabletop-scale experiments. *Science* **357**, 990–994 (2017).
11. Gregory, P. D., Blackmore, J. A., Bromley, S. L. & Cornish, S. L. Loss of ultracold $^{87}Rb^{133}Cs$ molecules via optical excitation of long-lived two-body collision complexes. *Phys. Rev. Lett.* **124**, 163402 (2020).
12. Hu, M. G. et al. Direct observation of bimolecular reactions of ultracold KRb molecules. *Science* **366**, 1111–1115 (2019).
13. Kirste, M. et al. Quantum-state resolved bimolecular collisions of velocity-controlled OH with NO radicals. *Science* **338**, 1060–1063 (2012).
14. Christianen, A., Zwierlein, M. W., Groenenboom, G. C. & Karman, T. Photoinduced two-body loss of ultracold molecules. *Phys. Rev. Lett.* **123**, 123402 (2019).
15. Danzl, J. G. et al. Quantum gas of deeply bound ground state molecules. *Science* **321**, 1062–1066 (2008).
16. Seeßelberg, F. et al. Extending rotational coherence of interacting polar molecules in a spin-decoupled magic trap. *Phys. Rev. Lett.* **121**, 253401 (2018).
17. Will, S. A., Park, J. W., Yan, Z. Z., Loh, H. & Zwierlein, M. W. Coherent microwave control of ultracold $^{23}Na^{40}K$ molecules. *Phys. Rev. Lett.* **116**, 225306 (2016).
18. Barry, J. F., McCarron, D. J., Norrgard, E. B., Steinecker, M. H. & Demille, D. Magneto-optical trapping of a diatomic molecule. *Nature* **512**, 286–289 (2014).
19. Truppe, S. et al. Molecules cooled below the Doppler limit. *Nat. Phys.* **13**, 1173–1176 (2017).
20. Anderegg, L. et al. An optical tweezer array of ultracold molecules. *Science* **365**, 1156–1158 (2019).
21. Ding, S., Wu, Y., Finneran, I. A., Burau, J. J. & Ye, J. Sub-Doppler cooling and compressed trapping of YO molecules at μK temperatures. *Phys. Rev. X* **10**, 021049 (2020).
22. Yang, H. et al. Observation of magnetically tunable Feshbach resonances in ultracold $^{23}Na^{40}K + {}^{40}K$ collisions. *Science* **363**, 261–264 (2019).
23. Son, H., Park, J. J., Ketterle, W. & Jamison, A. O. Collisional cooling of ultracold molecules. *Nature* **580**, 197–200 (2020).
24. Segev, Y. et al. Collisions between cold molecules in a superconducting magnetic trap. *Nature* **572**, 189–193 (2019).
25. Baranov, M. A., Dalmonte, M., Pupillo, G. & Zoller, P. Condensed matter theory of dipolar quantum gases. *Chem. Rev.* **112**, 5012–5061 (2012).

26. Aikawa, K. et al. Reaching Fermi degeneracy via universal dipolar scattering. *Phys. Rev. Lett.* **112**, 010404 (2014).
27. DeMarco, B. & Jin, D. S. Onset of Fermi degeneracy in a trapped atomic gas. *Science* **285**, 1703–1706 (1999).
28. Quéméner, G. & Bohn, J. L. Dynamics of ultracold molecules in confined geometry and electric field. *Phys. Rev. A* **83**, 012705 (2011).
29. Micheli, A. et al. Universal rates for reactive ultracold polar molecules in reduced dimensions. *Phys. Rev. Lett.* **105**, 073202 (2010).
30. Zhu, B., Quéméner, G., Rey, A. M. & Holland, M. J. Evaporative cooling of reactive polar molecules confined in a two-dimensional geometry. *Phys. Rev. A* **88**, 063405 (2013).
31. de Miranda, M. H. G. et al. Controlling the quantum stereodynamics of ultracold bimolecular reactions. *Nat. Phys.* **7**, 502–507 (2011).
32. Covey, J. P. *Enhanced Optical and Electric Manipulation of a Quantum Gas of KRb Molecules*. Thesis, Univ. Colorado, https://doi.org/10.1007/978-3-319-98107-9 (2018).
33. Shvarchuck, I. et al. Bose–einstein condensation into nonequilibrium states studied by condensate focusing. *Phys. Rev. Lett.* **89**, 270404 (2002).
34. Hueck, K. et al. Two-dimensional homogeneous Fermi gases. *Phys. Rev. Lett.* **120**, 060402 (2018).
35. Ni, K.-K. et al. A high phase-space-density gas of polar molecules. *Science* **322**, 231–235 (2008).
36. Quéméner, G. & Bohn, J. L. Strong dependence of ultracold chemical rates on electric dipole moments. *Phys. Rev. A* **81**, 022702 (2010).
37. Bohn, J. L., Cavagnero, M. & Ticknor, C. Quasi-universal dipolar scattering in cold and ultracold gases. *New J. Phys.* **11**, 055039 (2009).
38. Ticknor, C. Quasi-two-dimensional dipolar scattering. *Phys. Rev. A* **81**, 042708 (2010).
39. Bohn, J. L. & Jin, D. S. Differential scattering and rethermalization in ultracold dipolar gases. *Phys. Rev. A* **89**, 022702 (2014).
40. Aikawa, K. et al. Anisotropic relaxation dynamics in a dipolar Fermi gas driven out of equilibrium. *Phys. Rev. Lett.* **113**, 263201 (2014).
41. Babadi, M. & Demler, E. Collective excitations of quasi-two-dimensional trapped dipolar fermions: transition from collisionless to hydrodynamic regime. *Phys. Rev. A* **86**, 063638 (2012).
42. Giorgini, S., Pitaevskii, L. P. & Stringari, S. Theory of ultracold atomic Fermi gases. *Rev. Mod. Phys.* **80**, 1215 (2008).
43. Büchler, H. P. et al. Strongly correlated 2D quantum phases with cold polar molecules: controlling the shape of the interaction potential. *Phys. Rev. Lett.* **98**, 060404 (2007).
44. Góral, K., Santos, L. & Lewenstein, M. Quantum phases of dipolar bosons in optical lattices. *Phys. Rev. Lett.* **88**, 170406 (2002).
45. Capogrosso-Sansone, B., Trefzger, C., Lewenstein, M., Zoller, P. & Pupillo, G. Quantum phases of cold polar molecules in 2D optical lattices. *Phys. Rev. Lett.* **104**, 125301 (2010).
46. Cooper, N. R. & Shlyapnikov, G. V. Stable topological superfluid phase of ultracold polar fermionic molecules. *Phys. Rev. Lett.* **103**, 155302 (2009).
47. Gorshkov, A. V. et al. Tunable superfluidity and quantum magnetism with ultracold polar molecules. *Phys. Rev. Lett.* **107**, 115301 (2011).
48. Potter, A. C., Berg, E., Wang, D. W., Halperin, B. I. & Demler, E. Superfluidity and dimerization in a multilayered system of fermionic polar molecules. *Phys. Rev. Lett.* **105**, 220406 (2010).
49. Yao, N. Y. et al. Many-body localization in dipolar systems. *Phys. Rev. Lett.* **113**, 243002 (2014).
50. Barbiero, L., Menotti, C., Recati, A. & Santos, L. Out-of-equilibrium states and quasi-many-body localization in polar lattice gases. *Phys. Rev. B* **92**, 180406 (2015).
51. Zinner, N. T. & Bruun, G. M. Density waves in layered systems with fermionic polar molecules. *Eur. Phys. J. D* **65**, 133–139 (2011).
52. Peter, D., Müller, S., Wessel, S. & Büchler, H. P. Anomalous behavior of spin systems with dipolar interactions. *Phys. Rev. Lett.* **109**, 025303 (2012).

Methods

Experimental protocol

The experiment starts with an ultracold atomic mixture of ^{40}K and ^{87}Rb, held in the ODT at a magnetic field of 555 G. The trap frequencies for Rb in the ODT are $(\omega_x, \omega_y, \omega_z) = 2\pi \times (40, 180, 40)$ Hz. The atomic mixture is then transferred into a single layer of the LSL. The LSL beams propagate at a shallow angle of 4 degrees along **z**, resulting in a lattice spacing of 8 μm along **y**. At the end of the LSL ramp, we decrease the ODT power, so that the trap frequencies for Rb in the combined trap are $(\omega_x, \omega_y, \omega_z) = 2\pi \times (25, 600, 25)$ Hz. Typically, we have 4.1×10^5 K atoms and 7.0×10^4 Rb atoms at $T = 115(10)$ nK. About 30% of Rb is condensed. At this point, we load the mixture into the VL and adjust the ODT in order for the KRb molecules to experience radial trap frequencies at zero electric field of $(\omega_x, \omega_z) = 2\pi \times (40, 40)$ Hz, with $\omega_y/(2\pi)$ ranging from a few kilohertz up to 20 kHz. To compensate for the limited transmittivity of the ITO plates at the 1.064-μm VL wavelength and to avoid spurious superlattices, the VL beams have a 11-degree tilt with respect to **y**, resulting in a lattice spacing of 540 nm.

To create molecules, we first sweep the magnetic field adiabatically through the KRb heteronuclear Feshbach resonance at 546.6 G. The magnetic field is ramped from 555 G to 545.5 G in 4 ms, creating 2.5×10^4 Feshbach molecules that are subsequently transferred to the absolute KRb ground state by stimulated Raman adiabatic passage (STIRAP)[1]. By tuning the Raman lasers, we create KRb molecules at 0 kV cm^{-1} or 4.5 kV cm^{-1}. For molecule creation at 4.5 kV cm^{-1}, the field is ramped to the target value 10 ms before the Feshbach sweep. The STIRAP one-way transfer efficiency is 85(2)% at 0 kV cm^{-1} and 82(3)% at 4.5 kV cm^{-1}. We do not observe any dependence of β and S_{evap} on the initial value of the electric field.

Matter-wave focusing and layer counting

The VL layer spacing of 540 nm is too small to resolve with conventional absorption imaging. To quantify the number of occupied layers τ, we use a matter-wave technique that maps the in situ density distribution onto the momentum distribution, which can then be imaged in time of flight. To do so, we instantaneously release the cloud from the VL and the LSL into the ODT. The cloud expands into the ODT harmonic potential for a quarter of the oscillation period along **y**. This corresponds to a 90-degree rotation in phase space. As a result, after the rotation, the momentum distribution along **y** in time of flight corresponds to the original in-situ density profile. Increasing the time of flight increases the layer separation until they can be resolved optically. From a set of averaged matter-wave density profiles, we obtain a histogram with the normalized particle number per layer from which we extract the number of layers τ. We perform this analysis on a cloud of Rb atoms without K, eliminating the K–Rb interactions during the phase space rotation time. The Rb cloud used for matter-wave amplification imaging has the same trap parameters, number and temperature of the Rb cloud used for the molecule experiment. When the K–Rb interactions are removed by setting the magnetic field to the zero-crossing of the Feshbach resonance, the full contrast is restored. For the data in Fig. 1c, obtained by averaging 20 matter-wave images of the Rb cloud, the density histogram is shown in Extended Data Fig. 1. For a fixed molecule distribution, the definition of τ depends on the physical quantity being calculated. Using $\tau = N/\langle N_i \rangle$, where $\langle N_i \rangle$ is the average particle number per layer over the measured distribution, we extract $\tau = 4.6(2)$ for the data in Extended Data Fig. 1. Theoretical modelling[53] for the Rb cloud in the same conditions yields a consistent value of $\tau = 5.1(2)$.

Our measurements of the molecular cloud thus involve averaging over layers that are not equally populated. To determine T/T_{F}, we use the layer-averaged Fermi temperature $T_{\mathrm{F}} = \frac{\hbar\omega_{\mathrm{R}}}{k_{\mathrm{B}}}\sqrt{2}\sqrt{N_i} = \frac{\hbar\omega_{\mathrm{R}}}{k_{\mathrm{B}}}\left(\frac{2N}{\tau}\right)^{1/2}$, where $\tau = N/\sqrt{N_i}^2$ is an effective number of layers that accounts for the nonlinear dependence of T_{F} on N_i. For the data in Extended Data Fig. 1, we extract $\tau = 4.9(0.2)$. For the T/T_{F} data in the paper we thus use the closest estimate $\tau = 5 \pm 1$, where the uncertainty accounts for possible systematic errors arising from non-uniform conversion of Rb to KRb and variation of evaporation efficiency between the layers (since the density, and hence thermalization rate, varies between the layers).

To determine the 2D density for the measurement of β, we need to use a time-averaged layer number that considers the density dependence of the loss in each layer[3]. The layer-averaged 2D density is defined as $n = N/(4\pi\sigma^2\tau)$, where σ is the root-mean-square cloud size in the radial direction. Through numerical simulation, we obtain the decay over time for a cloud with the layer distribution plotted in Extended Data Fig. 1 and compare it with the decay of a gas with a uniform layer distribution and same number N. In this case, we define τ as the value for which β in the uniform case matches β in the non-uniform case. For Extended Data Fig. 1, we obtain $\tau = 8 \pm 1$.

Electric field potential

The anti-trapping potential that is used for dipolar evaporation introduces an anti-curvature that changes the trap frequency ω_x as a function of γ. Owing to the geometry of our electrodes, when $\gamma = 0.4225$ the electric field potential at the molecule position is as homogeneous as possible (fourth-order cancellation of the electric-field curvature). By increasing (decreasing) γ, ω_x decreases (increases), as shown in Extended Data Fig. 2 at $E_{\mathrm{DC}} = 5$ kV cm^{-1}. Our results follow the expected trend from finite-element simulations of the combined electro-optical potential at different γ.

Electric-field evaporation ramps

For the evaporation experiments, we lower the trap depth by increasing γ over time. The trap depth at each time point of the evaporation is estimated by simulations of the combined electro-optical potential, which is benchmarked with the measurement of ω_x versus γ displayed in Extended Data Fig. 2. For the data shown in Fig. 4, the evaporation ramp takes about 800 ms and E_{DC}, γ and trap depth evolve over time according to the plots in Extended Data Fig. 3. We also plot the trend of the parameter η and T/T_{F} at different time points of the evaporation sequence.

Thermometry of 2D Fermi gas

The 2D in situ density n of the molecular Fermi gas is given by the Fermi–Dirac distribution[54]:

$$n(x,z) = -\frac{1}{\lambda_{\mathrm{dB}}^2}\mathrm{Li}_1\left\{-\exp\left[-\beta_{\mathrm{th}}\left(\frac{1}{2}m\omega_x^2x^2 + \frac{1}{2}m\omega_z^2z^2 - \mu\right)\right]\right\}, \quad (3)$$

where m is the molecular mass, $\beta_{\mathrm{th}} = \frac{1}{k_{\mathrm{B}}T}$, μ the chemical potential, $\lambda_{\mathrm{dB}} = \sqrt{2\pi\hbar^2\beta_{\mathrm{th}}/m}$ the thermal de Broglie wavelength, and Li_n the polylogarithmic function of order n. The column-integrated density profile is:

$$n_{\mathrm{int}}(x) = -\frac{1}{\lambda_{\mathrm{dB}}^2}\sqrt{\frac{2\pi}{\beta_{\mathrm{th}}m\omega_z^2}}\mathrm{Li}_{3/2}\left\{-\exp\left[\beta_{\mathrm{th}}\left(\mu - \frac{1}{2}m\omega_x^2x^2\right)\right]\right\}. \quad (4)$$

After a certain time of flight t, the x coordinate scales by a factor $1/\sqrt{1+\omega_x^2t^2}$. The density is consequently divided by $\sqrt{1+\omega_x^2t^2}$ for proper renormalization. The chemical potential μ is defined through the relation:

$$\frac{N}{\tau} = \left(\frac{k_{\mathrm{B}}T}{\hbar\omega_{\mathrm{R}}}\right)^2\mathrm{Li}_2(-\mathrm{e}^{\beta_{\mathrm{th}}\mu}). \quad (5)$$

Combining equation (5) with the definition of T_{F} in 2D, we obtain:

$$\left(\frac{T}{T_{\mathrm{F}}}\right)^2 = -\frac{1}{2\,\mathrm{Li}_2(-\mathrm{e}^{\beta_{\mathrm{th}}\mu})}, \quad (6)$$

which allows us to extract the ratio T/T_{F} from the polylogarithmic fit.

From the Gaussian fit to the whole cloud, we obtain the Gaussian width σ and a release temperature T_{rel}, defined as:

$$T_{rel} = \frac{m\omega_x^2\sigma^2}{k_B(1+\omega_x^2t^2)}. \quad (7)$$

The release temperature T_{rel} is proportional to the energy density U of the Fermi gas, $U = 2k_BT_{rel}$, which saturates to a non-zero value as $T \to 0$. In contrast, the energy density $U_{cl} = 2k_BT$ of a classical gas approaches zero as $T \to 0$.

When the Gaussian fit is constrained to only the outer wings (that is, the high-momentum states) of the cloud, we can extract a new width σ_{out} from which, using equation (7), we obtain a corrected temperature T_{out} through the relation:

$$T_{out} = \frac{m\omega_x^2\sigma_{out}^2}{k_B(1+\omega_x^2t^2)}. \quad (8)$$

As the excluded region from the centre of the Gaussian fit is expanded, T_{out} decreases from an initial value of T_{rel} and approaches T. This is shown in Extended Data Fig. 4, where we plot the ratio T_{out}/T_{rel} at different exclusion regions in units of σ. For the range of T/T_F studied here, we find that an exclusion region of 1.5σ leaves us enough signal-to-noise ratio for the fit to properly converge and to return a value of T_{out} that is only 5% higher than T. In the main text, the Gaussian fit on the outer wings is performed with an excluded region of 1.5σ.

Data availability

The data that support the findings of this study are available from the corresponding author upon reasonable request. Source data are provided with this paper.

53. Dalfovo, F., Giorgini, S., Pitaevskii, L. P. & Stringari, S. Theory of Bose–Einstein condensation in trapped gases. *Rev. Mod. Phys.* **71**, 463–512 (1999).
54. Inguscio, M., Ketterle, W. & Salomon, C. Ultra-cold Fermi gases. In *Proceedings of the International School of Physics 'Enrico Fermi'* (2007).

Acknowledgements We acknowledge funding from NIST, DARPA DRINQS, ARO MURI and NSF Phys-1734006. We thank J. L. Bohn, A. M. Kaufman, and C. Miller for careful reading of the manuscript and T. Brown for technical assistance.

Author contributions All authors contributed to carrying out the experiments, interpreting the results, and writing the manuscript.

Competing interests The authors declare no competing interests.

Additional information
Correspondence and requests for materials should be addressed to G.V. or J.Y.
Peer review information *Nature* thanks Georgy Shlyapnikov and the other, anonymous, reviewer(s) for their contribution to the peer review of this work.
Reprints and permissions information is available at http://www.nature.com/reprints.

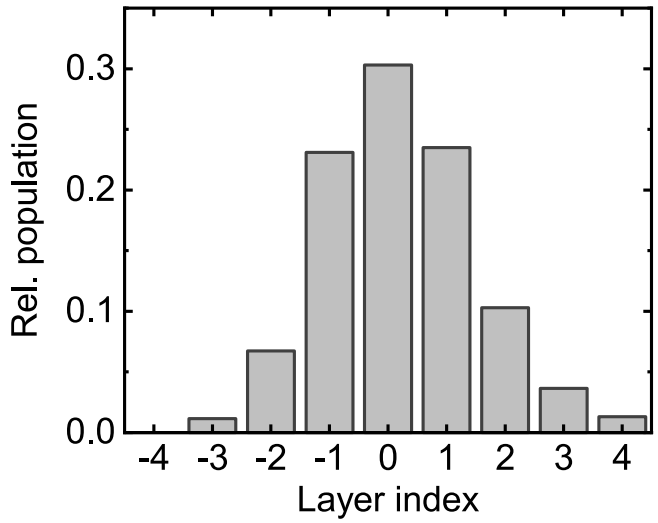

Extended Data Fig. 1 | Layer occupancy. Histogram of the average number per layer (relative population) for the data shown in Fig. 1c.

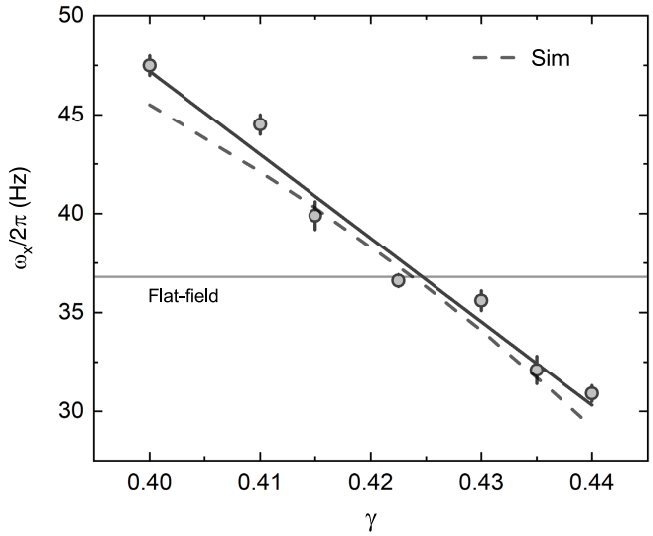

Extended Data Fig. 2 | Trend of $\omega_x/(2\pi)$ versus γ. Grey points are the experimental measurements at $E_{DC} = 5\,kV\,cm^{-1}$, the solid grey line is a linear fit to guide the eye, and the dashed line is the prediction (Sim) from the finite-element model. All error bars are 1 standard deviation of the mean.

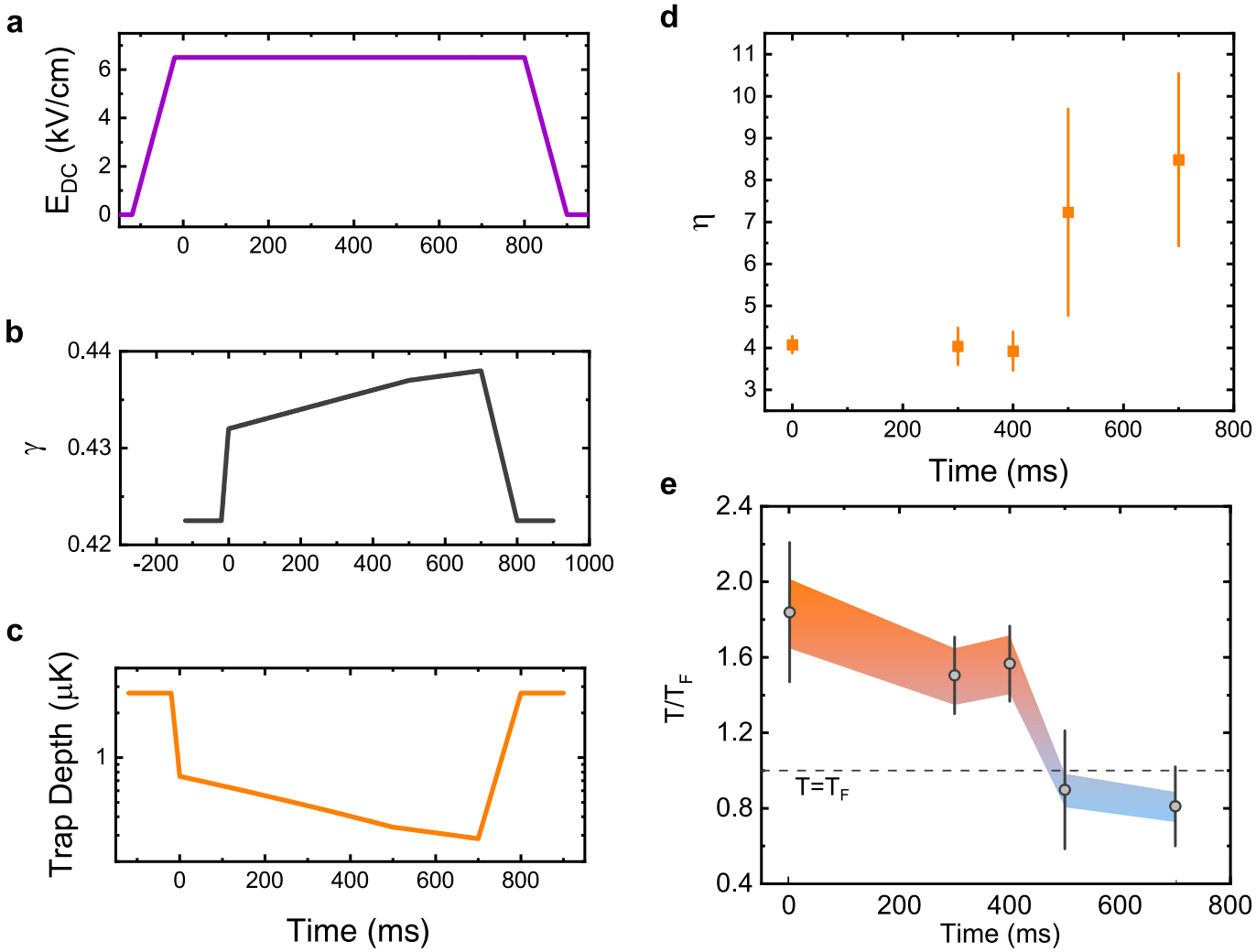

Extended Data Fig. 3 | Evaporation sequence. a, Ramp in E_{DC}. **b**, Ramp in γ. **c**, Trap depth versus time from the finite-element model of electro-optical potential. **d**, Evolution of η, calculated by taking the ratio of the trap depth and temperature at each time point. **e**, Evolution of T/T_F during the ramp. All error bars are 1 standard error of the mean.

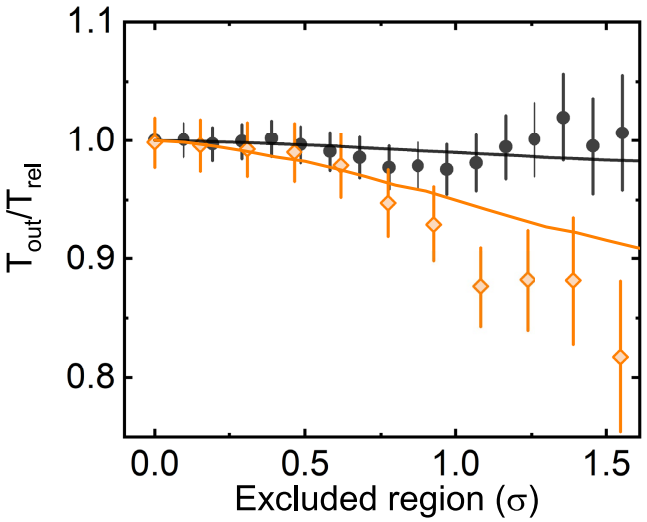

Extended Data Fig. 4 | Fermi gas thermometry. Trend of T_{out}/T_{rel} as a function of the excluded region from the centre of the Gaussian fit for $T/T_F = 0.81(15)$ (orange diamonds) and $T/T_F = 2.0(1)$ (black circles). Solid lines are Gaussian fits to simulated density profiles for $T/T_F = 2.0$ (black) and $T/T_F = 0.8$ (orange). All error bars are 1 standard error of the mean.